Journal of
Marine Science and Engineering

MDPI

Article

Numerical Simulations of a Ship's Maneuverability in Shallow Water

Jing Li [1,2], Qing Wang [3], Kai Dong [1,2] and Xianzhou Wang [1,2,*]

[1] School of Naval Architecture and Ocean Engineering, Huazhong University of Science and Technology, Wuhan 430074, China; l_jing@hust.edu.cn (J.L.); dong_kai@hust.edu.cn (K.D.)
[2] Key Laboratory of Ship and Ocean Hydrodynamics of Hubei Province, Wuhan 430074, China
[3] Wuhan Second Ship Design and Research Institute, Wuhan 430064, China; wangqing1037@163.com
[*] Correspondence: wangxz@hust.edu.cn

Abstract: It is necessary to maintain maneuverability for ship navigation in shallow water, such as channels, ports and other confined waters. In this study, a turning circle maneuver with 35° rudder deflection and a 20/5 zigzag maneuver for KVLCC2 in shallow waters are tested numerically to directly predict the maneuverability of the ship in shallow water. A viscous in-house CFD solver is applied with the dynamic overset grid approach. The impacts of the water depth on the ship's maneuverability in terms of turning and zigzag competence are evaluated, and the underlying mechanism is analyzed. The numerical method is validated by comparing it with experimental data on the turning indices, which shows good agreement. It is demonstrated that the turning capability become worse with a smaller depth–draft ratio, thus resulting in a lower yaw rate and a greater steady turning diameter. However, the drift angle and lateral speed are reduced with a smaller depth–draft ratio for zigzag maneuvers, but the overshoot angle and turn lag vary with the water depth non-monotonically.

Keywords: turning circle; zigzag; shallow water; CFD

check for updates

Citation: Li, J.; Wang, Q.; Dong, K.; Wang, X. Numerical Simulations of a Ship's Maneuverability in Shallow Water. *J. Mar. Sci. Eng.* **2024**, *12*, 1076. https://doi.org/10.3390/jmse12071076

Academic Editor: Lúcia Moreira

Received: 21 May 2024
Revised: 20 June 2024
Accepted: 21 June 2024
Published: 26 June 2024

1. Introduction

With an increase in ship displacement, many berths, ports and channel are becoming relatively smaller; thus, the water depth of these areas is restricted. Among these effect factors, including water depth, banks and ship-to-ship interactions, water depth is particularly important. The hydrodynamic performance will be significantly affected when ships navigate in shallow water, and the navigation attitudes and the forces acting on the ship change a lot in the form of increasing resistance, heave and trim. Moreover, maneuverability is significantly affected, thus decreasing safety. Although the design of commercial ships has been concentrated on the optimum resistance and propulsion systems to cut operational expenses, maneuverability has not been treated with equivalent consideration [1]. Also, inappropriate ship-handling on the part of navigating officers can lead to navigational casualties, such as contact, collision and grounding [2]. Thus, navigators should have a thorough understanding of a ship's maneuverability in shallow water in order to make informed decisions about how to maneuver a ship in shallow water. Therefore, it is of great importance to predict the maneuverability of ships navigating in shallow water and analyze the influence of water depth.

Over the past few decades, computational fluid dynamics (CFD) methods have made great contributions to predicting ship maneuverability, especially in deep water, owing to their efficiency and accuracy. Due to the importance of viscous effects for precise maneuverability predictions, unsteady Reynolds-averaged Navier–Stokes (URANS) simulations and detached eddy simulations (DESs) have been regarded the most promising methods instead of inviscid approaches. URANS simulations/DESs have replaced static and dynamic PMM (Planar Motion Mechanism) experiments in obtaining hydrodynamic derivatives and the details of the local flow around the hull during maneuvering [3]. The methods for predicting ship maneuverability when navigating in deep water have become relatively mature, including precise prediction in both waves and calm water, incorporating the influence of the maneuvering motion on the wake flow field and the propeller characteristics. Carrica et al. [4] utilized the CFD Ship-Iowa v4 solver to predict a ship's steady turn and zigzag maneuvers both in models and at the full scale. The results demonstrated that applying a URANS method to ship maneuverability prediction was suitable. Woolliscroft and Maki [5] presented a novel maneuvering prediction method to calculate the results accurately and significantly reduced the computational costs. Wang and Wan [6] numerically modelled the self-propulsion of a fully appended Office of Naval Research Tumblehome (ONRT) ship and carried out 10/10 zigzag maneuvers. The CFD results were in good agreement with the experimental results for both ship motions. This indicated the present method for predicting ship zigzag maneuvers in waves is feasible and reliable. Shen et al. [7] carried out RANS simulations of turning circle and zigzag maneuvers for DTMB 5415M, KVLCC2 (KRISO Very Large Crude Oil Carrier2) and KCS (the KRISO Container Ship) using a dynamic overset grid technique. Grids of the rudders and propellers were allowed to move and rotate about the ship hull, and the method could utilize relatively rough grids to carry out complex calculations. Suzuki et al. [8] improved the previous mathematical model that Hamamoto and Kim [9] proposed. They primarily improved the external wave forces and the inertial and damping parts of the hydrodynamic forces produced by the ship's motion so that the model could be employed in both short waves and for general maneuvers. Course-keeping and turning maneuvers of a tanker ship and a container ship navigating in regular waves were simulated numerically by applying the proposed method. Kinaci and Ozturk [10] carried out numerical simulations for the Duisburg Test Case (DTC) Post-Panamax container ship to investigate how the appendage forces affected its maneuvering abilities. The effects of a twisted rudder and the turning angle of the screw propeller on an asymmetric stern flow were mainly discussed. The results showed that the DTC inclined to starboard when the rudder was deflected to zero, and the rudder and propeller produced greater lateral forces acting on the starboard, causing the turning diameter to decrease in the port direction.

However, there are few studies on ship maneuverability when advancing at low speed in shallow water. Some researchers have used model testing methods constrained by numerical simulations to predict the maneuverability of ships [11–13]. A system-based maneuvering method was investigated by the researchers [14,15] in studying the maneuverability of ships. Tran Khanh et al. [14] proposed using a mathematical programming-based system identification method to optimize the nonlinear hydrodynamic coefficients. The optimal hydrodynamic coefficients were applied to simulate turning circle and zigzag maneuvers, and the numerical results were validated with experimental results. Du et al. [15] optimized the hydrodynamic coefficients of a tanker considering nonlinear ship–bank/bottom interactions. The optimal hydrodynamic coefficients were utilized in numerical simulations of turning circle and zigzag tests, and the differences between the experimental results and numerical results found well. On the basis of the MMG (Maneuvering Mathematical Modeling Group) model, Tang et al. [16] established a numerical model to simulate a ship's self-propulsion and turning and zigzag motions while accounting for the impact of shallow water. They compared the ship's motion trajectories at different depth–draft ratios, rudder angles and flow velocities under a non-uniform flow. The results demonstrated that the resistance would be increased and the maneuverability would decrease under the influence of shallow water. In addition, Carrica et al. [17] utilized a viscous flow method to conduct simulations of zigzag maneuvers in shallow water for KCS and evaluated the impact of the grid size on the predictable results by comparing them with the experimental results. Kim et al. [18] used a mathematical model to take into account the shallow water effect and study the maneuver characteristics of KVLCC2 when navigating in shallow water and deep water at low speed. They carried out a sensitivity analysis of the hydrodynamic derivatives to ascertain which had to be obtained precisely to avoid the constraints of the shallow water model applied in the previous study. Terziev et al. [19] compared the predictable motion parameters for the DTC container ship using several numerical methods, such as CFD, empirical methods and slender theory. In order to investigate the course-keeping stability of the KVLCC2 and DTC ships in shallow water with regard to various water depths, drift angles and angular velocities, Lee and Hong [20] used a CFD method to estimate the hydrodynamic derivative, analyzed the flow field and discussed the effect of non-linear influences.

The past research has mainly concentrated on the maneuverability of ships in deep water, while mostly indirect methods, such as model testing, system-based empirical methods and viscous flow methods, have been adopted to investigate the maneuverability of ships in shallow water by obtaining the hydrodynamic derivatives. In this work, direct viscous numerical simulations of turning circle and zigzag maneuvers for the KVLCC2 ship in very shallow water, shallow water and medium deep water are run using in-house viscous CFD code, with various depth–draft ratios of 1.2, 1.5 and 3.0, respectively. In addition, the results for very shallow water are validated with data from the SIMMAN2020 website [21]. During turning maneuvers, the six-DOF (degrees of freedom) motion of the ship and the influence of the water depth on the turning maneuverability of the ship, as well as the variation in the ship–propeller–rudder force at various water depths, are analyzed. For zigzag maneuvers, the influence of water depth on the ship's steering performance is analyzed. The impacts of different water depths on the hydrodynamic performance of the ship can provide a theoretical reference for other ships sailing in shallow waters, such as ports and coastal waters, so as to improve safety performance during maneuvering.

2. Model and Simulation Conditions

2.1. The KVLCC2 Model

The International Towing Tank Conference (ITTC) benchmark ship hull KVLCC2 with a scale ratio of 1/75 is used in this work, as shown in Figure 1, and the main particulars at both the model scale and full scale are listed in Table 1. The ship model is equipped with a single starboard propeller and a single rudder, as shown in Figure 2. The position of the propeller surface is at 0.98 $\mathrm{L_{PP}}$, and the position of the rudder shaft is at 1.0 $\mathrm{L_{PP}}$. The main particulars of the propeller are listed in Table 2.

Table 1. Main particulars of the KVLCC2 model and full scale.

Parameter	Symbol	Full Scale	Model Scale	Units
Scale ratio	λ	1	1/75	-
Length of perpendicular	L_{pp}	320	4.267	m
Length of waterline	L_{wl}	325.5	4.34	m
Maximum beam of waterline	B_{wl}	58	0.7733	m
Depth	D	30	0.4	m
Draft	T	20.8	0.2773	m
Displacement	∇	312,622	0.741	m^3
Wetted surface area	Sw	27,194	4.835	m^2
Block coefficient	C_B	0.8098	0.8098	-
Midship section coefficient	C_M	0.998	0.998	-
Distance from center of buoyancy to midship	L_{CB}	3.48	3.48	-
Distance from center of gravity to midship	L_{CG}	171.1	2.281	m
Metacentric height	GM	5.71	0.0752	m
Inertia radius about X-axis	i_{xx}/B	0.4	0.4	-
Inertia radius about Y-axis	i_{yy}/L_{pp}	0.25	0.25	-
Inertia radius about Z-axis	i_{zz}/L_{pp}	0.25	0.25	-
Rudder total wetted area	S_R	273.3	0.0486	m^2
Rudder rate	-	2.32	20.09	deg/s

Figure 1. KVLCC2 model.

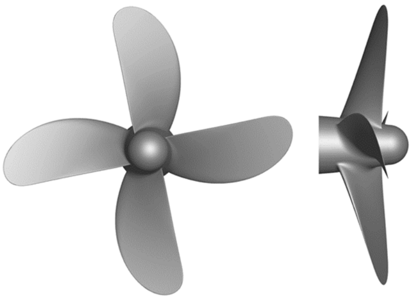

Figure 2. Starboard propeller model.

Table 2. Main particulars of KVLCC2 propeller model and full scale.

Parameter	Symbol	Full Scale	Model Scale	Units
Scale ratio	λ	1	1/75	-
Propeller diameter	D_P	9.86	0.13	m
Pitch ratio (0.7R)	P/D (0.7R)	0.721	0.721	-
Area ratio	A_e/A_0	0.431	0.431	-
Hub ratio		0.155		-
Rotation	-	Right hand	Right hand	-

2.2. Simulation Conditions

According to the definition of shallow water and deep water proposed by the World Association for Waterborne Transport Infrastructure [22], maneuvers with a 35° turning circle and a 20/5 zigzag are simulated numerically in very shallow water (h/T = 1.2), shallow water (h/T = 1.5) and medium deep water (h/T = 3.0) conditions. The simulation conditions of the ship model are shown in Table 3.

Table 3. Simulation conditions of the ship model.

Case	h/T [-]	Velocity [m/s]	Fn [-]	λ [-]	Rudder Rate [°/s]	Maximum Rudder Deflection [°]	Maneuver [-]
1	1.2	0.415	0.064	1/75	2.32	35	Turning Circle
2	1.5						
3	3.0						
4	1.2	0.415	0.064	1/75	2.32	20, 5	Zigzag
5	1.5						
6	3.0						

3. Computational Method

3.1. Six-DOF Equations

During the maneuvers of turning and zigzag, the ship is affected by external forces in the flow field, which then cause changes in navigation attitude. The six-degrees-of-freedom motion model of the ship in the in-house CFD code is described by the following equations:

$$\mathrm{m}\left[\dot{u} - vr + wq\right] = X \tag{1}$$

$$\mathrm{m}\left[\dot{v} - wp + ur\right] = Y \tag{2}$$

$$\mathrm{m}\left[\dot{w} - uq + vp\right] = Z \tag{3}$$

$$I_x\dot{p} + \left[I_y - I_z\right]qr = K \tag{4}$$

$$I_y\dot{q} + \left[I_x - I_z\right]rp = M \tag{5}$$

$$I_z\dot{r} + \left[I_z - I_x\right]pq = N \tag{6}$$

where m is the ship's mass; u, v, w and p, q, r are the translational velocity along the three coordinate axes and the angular velocity around the three coordinate axes; X, Y, Z and K, M, N are the forces and the moments exerted on the ship hull; I_x, I_y and I_z are the ship's moments of inertia around the three axes in the ship-fixed coordinate system. There are two right-handed Cartesian coordinate systems applied to describe the 6-DOF motion of the ship: a ship-fixed coordinate system $O_S - X_SY_SZ_S$, whose original point O_S is located at the ship's center of gravity, and an Earth-fixed coordinate system $O_E - X_EY_EZ_E$, whose original point O_S is located at the intersection of the ship's design waterline and bow perpendicular, as shown in Figure 3. The $O_S - X_S$ axis points positively from the ship's bow to its stern, the $O_S - Y_S$ axis points positively to starboard and the $O_S - Z_S$ axis points positively upward vertically. At the initial moment, the axes of both coordinate systems point in the same direction; the output results on the ship's 6-DOF motion are based on the Earth-fixed coordinate system, and the predictable results on the forces and moments acted on the ship are based on the ship-fixed coordinate system. The forces and moments in Equations (1)–(6) were calculated using the integrals of pressure and stress terms along the ship. They were acquired in the Earth-fixed coordinate system first and then were transformed for the non-inertial ship-fixed coordinate system.

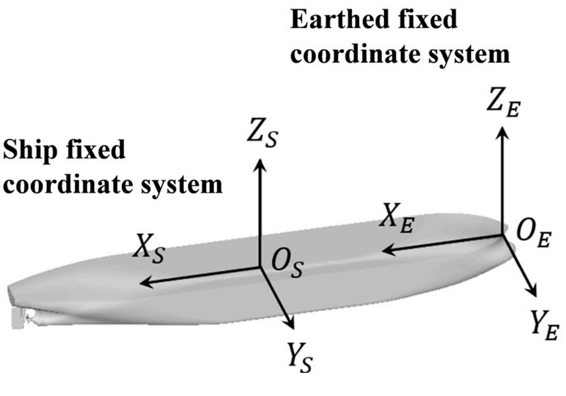

Figure 3. Two coordinates.

3.2. Governing Equations and the Propulsion Model

To solve the 6-DOF equations for the ship, URANS equations for an incompressible fluid are solved using the in-house CFD code. The RANS equations, coupled with the continuity equation, are shown as follows:

$$\frac{\partial \rho}{\partial t} + \frac{\partial (\rho U_i)}{\partial x_i} = 0 \tag{7}$$

$$\frac{\partial U_i}{\partial t} + U_j \frac{\partial U_i}{\partial x_j} = -\frac{1}{\rho}\frac{\partial P}{\partial x_i} + \frac{1}{\rho}\frac{\partial}{\partial x_j}\left(\mu \frac{\partial U_i}{\partial x_j} - \rho\overline{u_i u_j}\right) + f^*_{b_i} \tag{8}$$

where U_i is the temporal mean velocity, μ is the dynamic viscosity, $\rho\overline{u_i u_j}$ is the Reynolds stress, u_i is the fluctuating velocity, P is the pressure and $f^*_{b_i}$ is the body-force source term. The URANS equations are solved using the two-equation shear stress transport turbulence model (SST k-ω) proposed by Menter [23]. It has been demonstrated that the (SST k-ω) turbulence model is effective in predicting adverse pressure gradients and separation flows, which are crucial issues in maneuvering simulations. The in-house CFD code applies the finite difference method (FDM) to discretize the URANS equations. Temporal terms are discretized using an implicit Euler backward difference scheme with a second-order accuracy scheme. The convective terms and the non-cross viscous terms for the spatial terms are discretized using Total Variation Diminishing and second-order central difference schemes, respectively. The free surface is calculated using the level-set approach [24]. Moreover, the body-force source term is added to the momentum equations in order to model the propeller instead of using a discrete propeller model, which can obviously save the computational time and increase the efficiency. The Osaka University Method (OUM) raised by [25], based on the infinite-bladed propeller model, is applied in this numerical method and was validated in earlier works [26–28].

3.3. The PI Speed Controller

In order for the ship to reach a certain speed during self-propulsion, the PI (Proportional–Integral) speed controller Carrica et al. [1] adjusts the propeller's rotational speed until the target speed is achieved. The propeller's rotating speed n is shown as follows:

$$n = K_p e + K_i \int_0^t e dt \tag{9}$$

where $e = U_{target} - U_{ship}$ is the difference between the current ship velocity U_{ship} and the target velocity U_{target}; K_p is the proportional constant; K_i is the integral constant. The empirical formula to obtain K_p and K_i is shown as follows:

$$K_p = K_i = \frac{\frac{n}{\Delta t}}{500} \tag{10}$$

where Δt is the time step. Increasing the value of K_p can adjust the propeller's rotational speed to the target speed faster, but it will lead to increasing flotation. The function of K_i is applied to eliminate errors.

3.4. Grid Generation

In this study, grids of the computational domain, the ship, refinement, the rudder and the rudder root are generated independently and then are combined into a structured overset grid system using an in-house overset grid method [27]. The grids in the overset system overset each other with one or more grids Rogers et al. [29]. The grids of the computational domain are shown in Figure 4. The purpose of Refine 1 is to provide fine grids around ship, thus ensuring numerical stability and accuracy. Refine 2 is set to solve the local flow field precisely while deflecting the rudder. A view of the grids around the ship is given in Figure 5. Also, fine meshes around the ship hull and the rudder can clearly be observed in Figure 5. The overset grids before and after oversetting are shown in Figures 6 and 7.

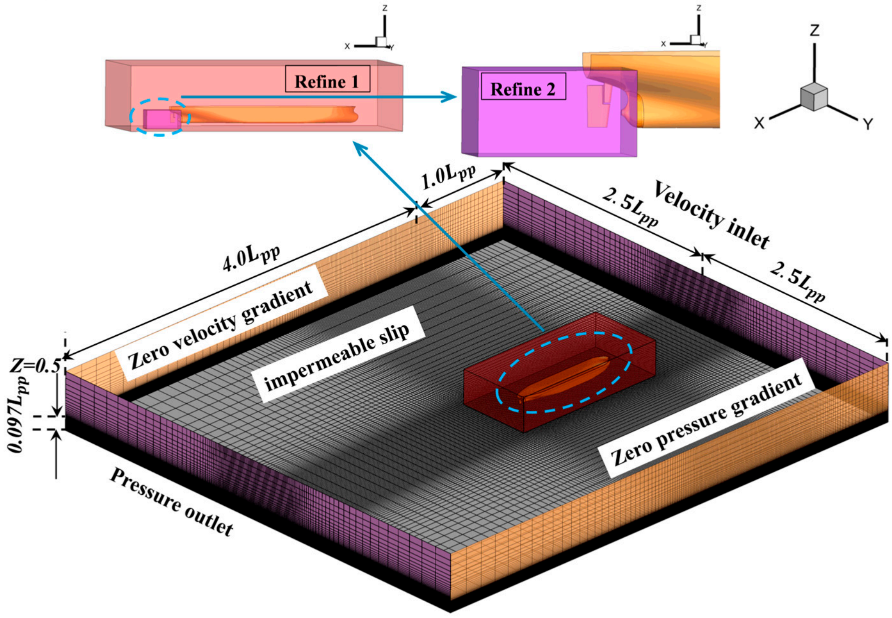

Figure 4. The dimensions and boundary conditions of computational domain in very shallow water.

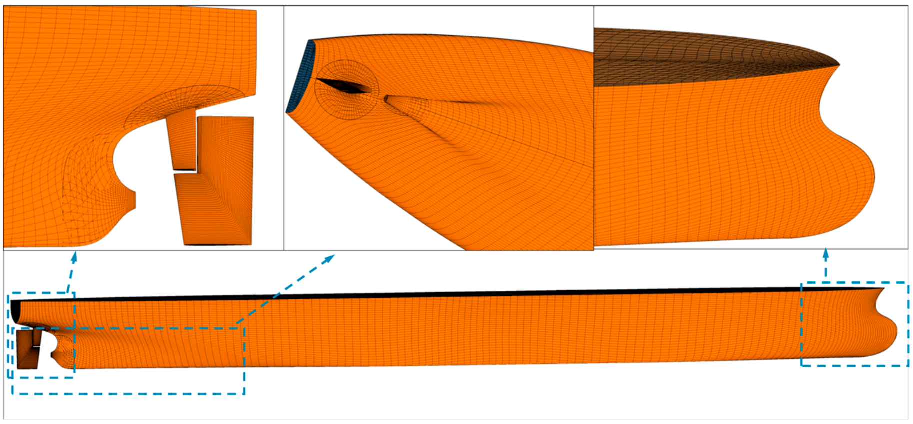

Figure 5. A general view of the grids around the ship.

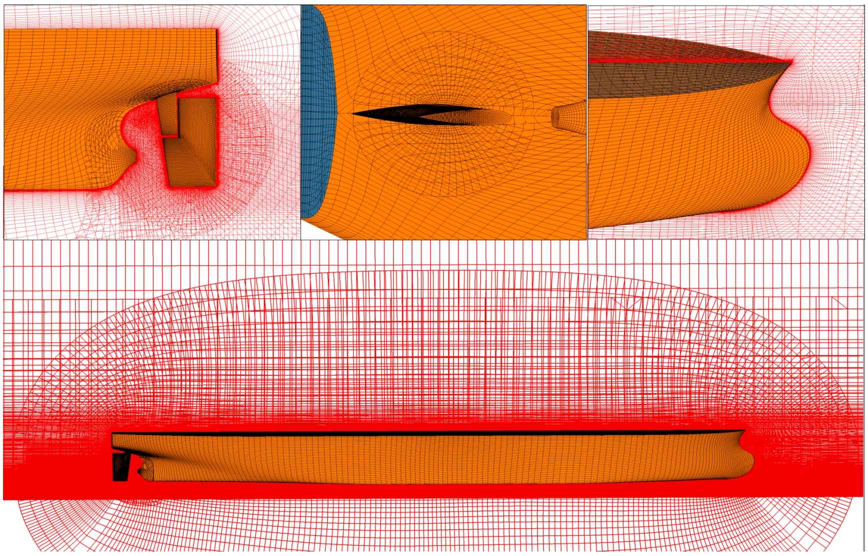

Figure 6. Overset grids (before oversetting).

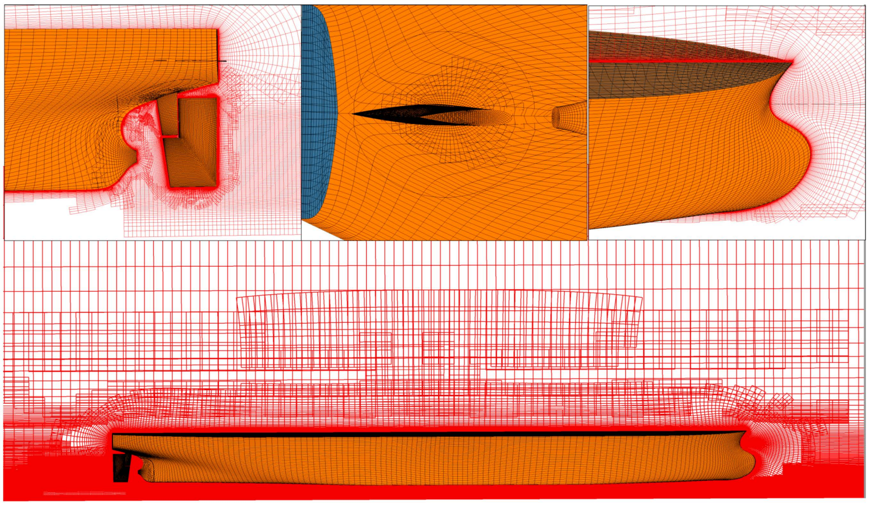

Figure 7. Overset grids (after oversetting).

The computational domain extends over the ranges of $-1 < x/L_{PP} < 4$, $-2.5 < y/L_{PP} < 2.5$, and the depth of the computational domain is determined according to the specific water depth conditions. Taking very shallow water (h/T = 1.2) as an example, $0.0780 < z/L_{PP} < 0.3$ (where $h/L_{PP} = 0.0780$). The length of the ship is aligned with the x-axis with the bow at x = 0 and the stern at $x = L_{PP}$. The initial free surface is located at $Z = 0$. The boundary conditions of the computational domain are displayed in Figure 7. A pressure outlet condition is imposed at the outlet boundary. The bottom boundary is set as an "impermeable slip" condition, while in deep water simulations, it is typically configured as a "zero dynamic pressure" boundary condition [26]. The top boundary was set as a "zero pressure gradient" condition. Both side boundaries were set to "zero velocity gradient" conditions, which means constant velocity boundary conditions.

4. Verification and Validation of the Numerical Method

In this section, verification of the numerical method for the KVLCC2 model's resistance in deep water (h/T > 3.0) and shallow water (h/T = 1.5) and validation of turning tests in shallow water (h/T = 1.5) were carried out. The uncertainties of the numerical method were estimated by applying the ASME V&V (Verification and Validation) procedure [30]. The aim of the verification procedure is to ascertain the uncertainty of the numerical method U_{SN}, while the validation process is used to compare the numerical results with the experimental results. It should be noted that a KVLCC2 model appended with a rudder was used in the convergence study of the deep water conditions, but a bare KVLCC2 model was applied in the convergence study of the shallow water conditions. The selection of different ship models in the convergence study allowed us to match the scale ratio of the experimental ship model. Therefore, whether the grids of the rudder and the rudder root are reasonable could be examined through studying the uncertainty in deep water conditions.

4.1. Verification Study

In the verification study, convergence studies on the grids and time steps were implemented using the Richardson extrapolation method recommended by Xing and Stern [31], in which the numerical uncertainty U_{SN} is composed of uncertainty from iteration U_I, grid U_G, time step U_T and other parameters U_P. Herein, U_I and U_P can be ignored, so the numerical uncertainty is as follows:

$$U_{SN}{}^2 = U_G{}^2 + U_T{}^2 \tag{11}$$

Convergence studies on the grids and time steps are accomplished using at least three solutions for the grids and time steps with systematic refinement, including coarse, medium and fine sizes. A refinement ratio r_k of $\sqrt{2}$ is used according to the recommendations of the ITTC.

The convergence ratio R is defined as follows:

$$R = \frac{\varepsilon_{32}}{\varepsilon_{21}} \tag{12}$$

where $\varepsilon_{32} = S_f - S_m$, $\varepsilon_{21} = S_m - S_c$, S_c, S_m, S_f are the results using coarse, medium and fine grids or time steps, respectively. The value of R reflects different convergence conditions. When $0 < R < 1$, monotonic convergence is achieved, and the Richardson extrapolation method can be used. The estimated order of accuracy P_{RE} was calculated as follows:

$$P_{RE} = \frac{\ln(\varepsilon_{21}/\varepsilon_{32})}{\ln r_k} \tag{13}$$

$$P = \frac{P_{RE}}{P_{th}} \tag{14}$$

where P is the distance metric; P_{th} is an estimate of the limiting order of accuracy as the spacing size goes to zero; generally, P_{th} = 2 [32]. The factor of safety method uncertainty is given as follows:

$$U_{FS} = \begin{cases} (2.45 - 0.85P)\left|\frac{S_f - S_m}{{r_k}^{P_{RE}} - 1}\right|, & 0 < P \leq 1 \\ (16.4P - 14.8)\left|\frac{S_f - S_m}{{r_k}^{P_{RE}} - 1}\right|, & P > 1 \end{cases} \tag{15}$$

When $-1 < R < 0$, oscillational convergence is achieved. Then, the relative uncertainty U_K can be estimated as follows:

$$U_K = \frac{1}{2}\left(S_U - S_L\right) \tag{16}$$

where S_U and S_L refer to the maximum and minimum of the solutions, respectively.

The convergence studies for the grids and time steps were conducted by verifying the total resistance coefficient in deep water, with Froude number (Fn) = 0.142 at a scale ratio of 1/45.714, and in shallow water, with a Fn = 0.064 at a scale ratio of 1/75. The grid convergence study results on the total resistance coefficients at both water depths are shown in Tables 4–7, where EFD refers to the experimental total resistance coefficient [33,34]. Three sizes of grids and time steps with a refinement ratio of $\sqrt{2}$ are applied to evaluate the convergence. It can be found that the influence of the grid number on the total resistance coefficient is slighter than that of the time step size. Moreover, the differences between grid sizes are small, but the coarse time step exhibits a significant difference as compared with the solutions for the medium and fine time steps. Therefore, a model with medium grid and medium time step sizes should be utilized for subsequent studies to guarantee accurate calculations and reduce the calculation time. The numerical uncertainty results are shown in Table 8.

Table 4. Grid convergence study of total resistance coefficient in deep water (h/T > 3.0, Fn = 0.142).

Grid Solution	Coarse	Medium	Fine
Total grid number [M]	1.36	3.85	10.90
Total resistance coefficient [-]	3.908×10^{-3}	4.015×10^{-3}	4.035×10^{-3}
EFD [-]	4.050×10^{-3}	4.050×10^{-3}	4.050×10^{-3}
Difference [%D]	−3.50	−0.86	−0.36
R_G [-]		0.1869	
P [-]		2.417	
Convergence type		Monotonic convergence	
U_G [%D]		2.821	

Table 5. Grid convergence study of total resistance coefficient in shallow water (h/T = 1.5, Fn = 0.064).

Grid Solution	Coarse	Medium	Fine
Total grid number [M]	1.44	4.07	11.51
Total resistance coefficient [-]	8.981×10^{-3}	8.759×10^{-3}	8.664×10^{-3}
EFD [-]	8.530×10^{-3}	8.530×10^{-3}	8.530×10^{-3}
Difference [%D]	5.29	2.69	1.57
R_G [-]		0.1869	
P [-]		2.417	
Convergence type		Monotonic convergence	
U_G [%D]		2.821	

Table 6. Time step convergence study of total resistance coefficient in deep water (h/T > 3.0, Fn = 0.142).

Time Step Solution	Coarse	Medium	Fine
Time step [s]	0.0209	0.0148	0.0105
Total resistance coefficient [-]	3.942×10^{-3}	4.015×10^{-3}	4.044×10^{-3}
EFD [-]	4.050×10^{-3}	4.050×10^{-3}	4.050×10^{-3}
Difference [%D]	−2.66	−0.86	−0.14
R_T [-]		0.3973	
P [-]		1.341	
Convergence type		Monotonic convergence	
U_T [%D]		3.395	

Table 7. Time step convergence study of total resistance coefficient in shallow water (h/T = 1.5, Fn = 0.064).

Time Step Solution	Coarse	Medium	Fine
Time step [s]	0.0363	0.0257	0.0182
Total resistance coefficient [-]	8.931×10^{-3}	8.759×10^{-3}	8.676×10^{-3}
EFD [-]	8.530×10^{-3}	8.530×10^{-3}	8.530×10^{-3}
Difference [%D]	4.70	2.69	1.71
RG [-]		0.4826	
P [-]		1.055	
Convergence type		Monotonic convergence	
UT [%D]		4.252	

Table 8. Numerical uncertainty of total resistance coefficient in deep water and shallow water.

Uncertainty	Deep Water Conditions	Shallow Water Conditions
U_G [%D]	2.821	4.408
U_T [%D]	3.395	4.252
U_{SN} [%D]	4.414	6.124

4.2. Validation

The sizes of the grid and time step were confirmed in Section 4.1. The total resistance coefficient in shallow water is compared with the experimental data [33], and that in deep water is compared with the experimental data [34] to evaluate the numerical method.

The comparison error E is defined as

$$E = D - S \tag{17}$$

where D is the experimental data and S is the numerical result for the medium-grid and medium-time-step model. E is compared to the validation uncertainty U_V to ascertain whether validation has been accomplished. U_V is provided by:

$$U_V^2 = U_D^2 + U_{SN}^2 \tag{18}$$

If $|E| < U_V$, validation of the uncertainty analysis is complete. The uncertainty of the experimental data U_D was not known, and hence U_D was assumed as 1.00%D. The results of the validation study are shown in Table 9. According to $|E| < U_V$ in deep water and shallow water conditions, the numerical method was validated at the U_V level. Therefore, the numerical method is stable and reliable for subsequent numerical simulations.

Table 9. Results of validation study on the total resistance coefficient.

Water Conditions	U_{SN} [%D]	U_D [%D]	U_V [%D]	E [%D]
Deep water	4.414	1.000	4.526	−0.86
Shallow water	6.124	1.000	6.205	2.69

The above verification and validation process demonstrated that the present numerical approach is appliable to predicting the resistance of ships in shallow water. Meanwhile, in order to validate the accuracy of the numerical method in predicting a ship's maneuverability when advancing at low speed (Fr = 0.064) in very shallow water, 35° turning parameters for KVLCC2 under very shallow water conditions (h/T = 1.2) are compared with the experimental data, including the turning trajectories, as well as time series of the yaw angle, speed, drift angle and roll angle. The experimental data provided on the SIMMAN2020 website, including the full-scale linear and angular velocities in the X and Y directions, were converted according to a scale ratio of 1/75 using a characteristic speed and length for comparison with the numerical results. Figure 8 displays a comparison of the numerical and experimental results, including the turning trajectory, yaw rate, speed, drift angle and roll angle. The differences between the numerical and experimental results are presented in Table 10.

Table 10. Numerical uncertainty for turning maneuvering parameters.

	Ad [m]	Tr [m]	D_{t90° [m]	φ_{90° [deg]	r_{90° [deg/s]	β_{90° [deg]	$\frac{(\Delta u)_{90^\circ}}{u_0}$ [%]
EFD	12.07	8.893	18.82	−0.2039	2.073	2.000	78.13
CFD	13.06	9.854	20.12	−0.1420	1.808	2.241	76.38
Diff. [%]	8.20	10.81	6.91	−30.36	−12.78	12.05	−2.24

Ad: advance. Tr: transfer. D_{t90°: instantaneous tactical diameter when the yaw angle turns to 90°. φ_{90°: the roll angle when the yaw angle turns to 90°. r_{90°: the yaw rate when the yaw angle turns to 90°. β_{90°: the drift angle when the yaw angle turns to 90°. $\frac{(\Delta u)_{90^\circ}}{u_0}$: the speed loss index when the yaw angle turns to 90°.

It should be noted that the experimental data provided by the SIMMAN2020 website only contain data for a ship heading angle of 100°, in which the turning indices are not stable. Herein, the yaw rate, velocity, drift angle and roll angle when the ship's yaw angle turns to 90° in the numerical and experimental results are compared in this section. The instantaneous tactical diameter D_t is defined as the diameter of the ship's turning circle in the period of Δt before and after a given moment. The expression of the instantaneous tactical diameter D_t is

$$D_t = \frac{2\Delta L}{\Delta \theta} \tag{19}$$

where ΔL and $\Delta \theta$ are the arc length and the central angle of the turning circle during the Δt period, respectively.

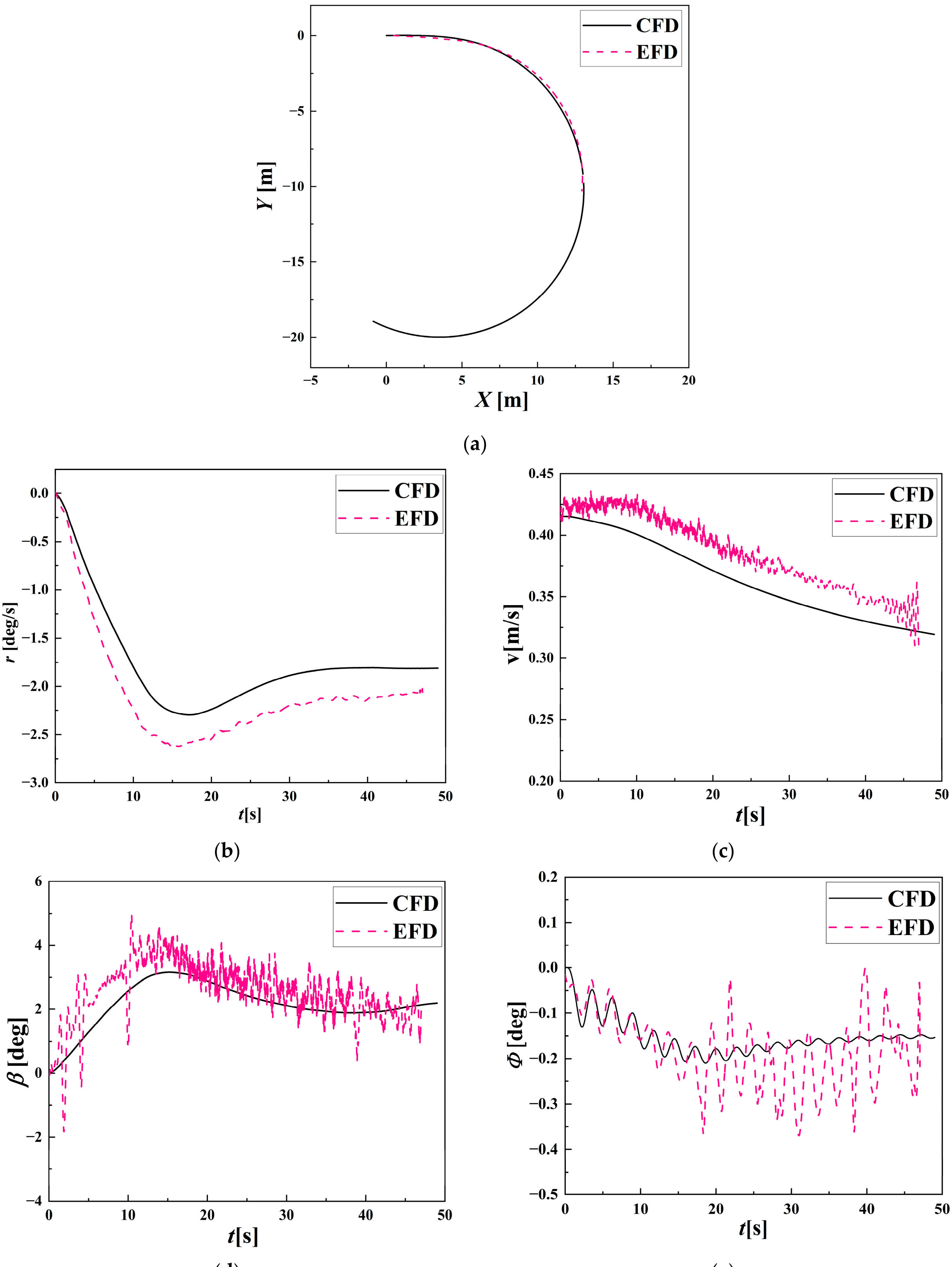

(**a**)

(**b**) (**c**)

(**d**) (**e**)

Figure 8. Turning trajectories and time series of motions for CFD and experimental results: (**a**) turning trajectories; (**b**) yaw rate; (**c**) velocity; (**d**) drift angle; (**e**) roll angle.

It can be observed from Table 10 that all the differences between the numerical results and experimental results are less than 13%, except for the difference in the roll angle, in which a small roll angle results in a larger relative error. Generally, the present numerical method can be used to predict the maneuverability of KVLCC2 navigating in shallow water.

5. Results and Discussion

Turning and zigzag maneuvers of 1/75 KVLCC2 were simulated in very shallow water (h/T = 1.2), shallow water (h/T = 1.5) and medium deep water (h/T = 3.0) conditions, respectively. The indices of the turning and zigzagging motions and the performance of the propeller at various water depths will be analyzed in this section.

5.1. Results of Ship Performance during Self-Propulsion

The ship is propellered to the velocity point of 0.415 m/s with only heave and pitch motion released before steering. The results on self-propulsion in different water conditions are shown in Table 11.

Table 11. Results on KVLCC2's self-propulsion at different water depths.

Water	h/T	n [rps]	K_T	T [N]	K_Q	Q [N·m]	t [-]	η
Very shallow water	1.2	7.756	0.2565	4.536	0.02499	0.05788	0.1746	0.4257
Shallow water	1.5	7.551	0.2337	3.917	0.02423	0.05321	0.1900	0.5132
Medium deep water	3.0	7.137	0.2182	3.267	0.02347	0.04603	0.2110	0.5647

where $K_T = \frac{T}{\rho n^2 D^4}$, $K_Q = \frac{Q}{\rho n^2 D^5}$, n is the rotating speed of propeller, T is the propulsion force, Q is the torque coefficient of propeller, D is the diameter of propeller, K_T is the thrust coefficient of propeller, K_Q is the torque coefficient of propeller, t is the thrust deduction of propeller and η is the efficiency of propeller.

Due to the impact of the background bottom, the resistance force is equal to the propulsion force and notably increases in shallower water. The rotating speed of the propeller in very shallow water is 9% higher than that in medium deep water. A higher rotating speed is required for the propeller to provide enough propulsion force in order to achieve the same velocity in shallower water. Meanwhile, the thrust deduction and the efficiency of the propeller decrease with shallower water. The stern flow attenuates rapidly due to the influence of the boundary layer at the background bottom under very shallow water conditions, and this influence is weakened in deeper water, which is consistent with Figure 9a. Figure 9b represents the flow field at the stern, which shows the great difference in the flow field around the rudder between the water conditions. The flow of the propeller is close to the two sides of the rudder in very shallow water, while the flow separates from the two sides of the rudder when the water depth increases.

The amplitude of wave-making during self-propulsion is shown in Figure 10. Figure 10 represents a similar principle for resistance, which indicates greater wave-making in shallower water. The heave and pitch amplitudes during self-propulsion are shown in Table 12. The amplitudes of heave and pitch motion also rise in shallower water, and shallow water affects the heave motion more than the pitch motion.

Table 12. The amplitudes of heave and pitch motion during self-propulsion.

Condition	h/T	Heave [m]	Pitch [deg]
Very shallow water	1.2	-2.929×10^{-3}	-3.629×10^{-2}
Shallow water	1.5	-2.153×10^{-3}	-2.923×10^{-2}
Medium deep water	3.0	-1.192×10^{-3}	-2.216×10^{-2}

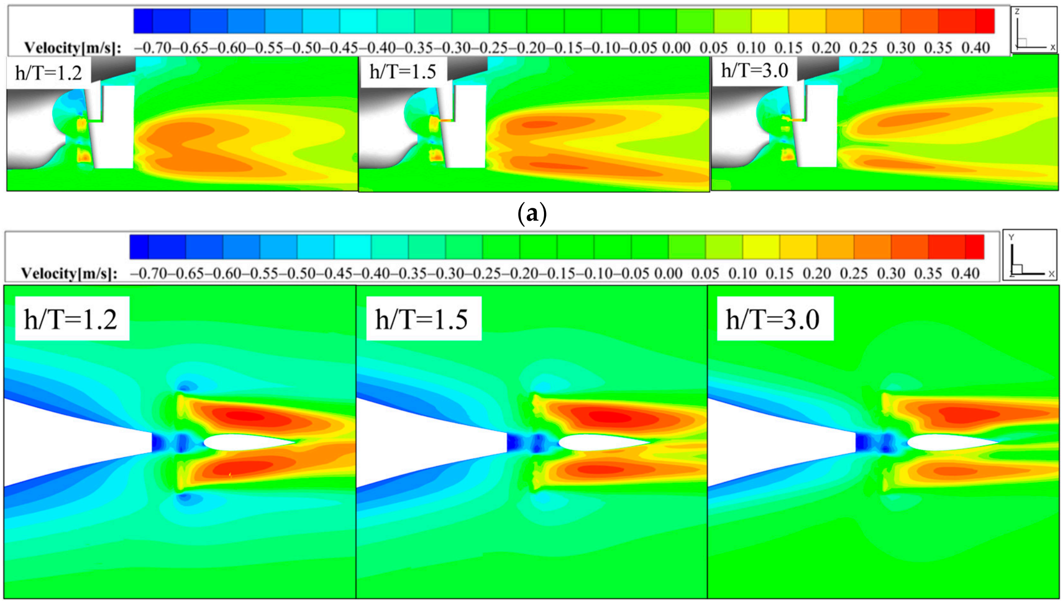

(**a**)

(**b**)

Figure 9. The flow field at stern during the self-propulsion process in different water conditions. (**a**) XOZ plane; (**b**) XOY plane.

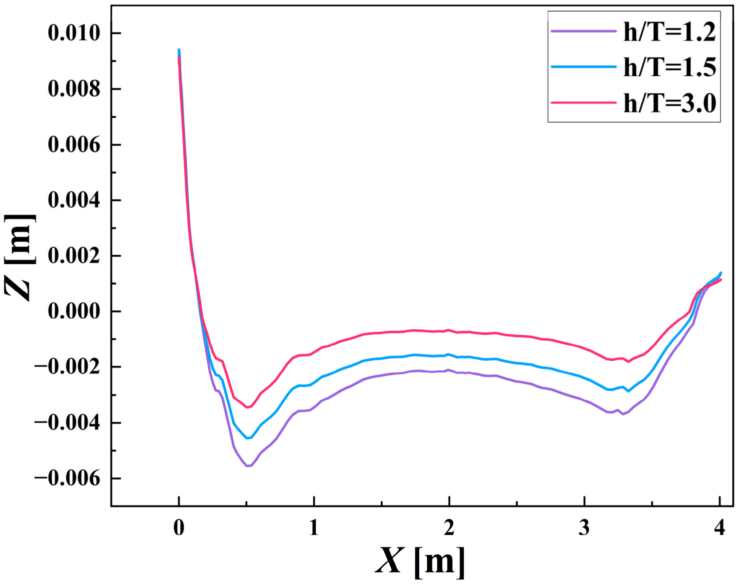

Figure 10. The amplitude of wave-making during self-propulsion process in different water conditions.

5.2. Results on the Turning Maneuver at Different Water Depths

5.2.1. Turning Indices of Different Water Depths

The turning indices under different water depths are compared and analyzed in this section. The ship model is propelled to the self-propulsion point with a velocity of 0.415 m/s corresponding to a Froude number = 0.064 before steering. Then, the ship model turns to the starboard side on account of the 35° rudder deflection with a rudder rate = 20.09°/s (corresponding to 2.32°/s at full scale). Finally, the ship generally enters a steady turning state. The turning circles, the time series of the total resistance and propulsion force and motions for the turning maneuvers in very shallow water/shallow water/medium deep water are shown in Figure 11. The parameters for the turning maneuver are shown in Table 13, which shows significant differences in the turning parameters at different water depths. The steady turning diameter increases and the amplitude of the yaw rate decreases with a smaller depth–draft ratio, which indicates a worse turning performance. Further, the steady turning diameter in very shallow water is 1.4 times that in shallow water and 1.8 times that in medium deep water. Significant differences in the yaw rate amplitude exist at various water depths, while there is only a small difference in the steady yaw rate. Time series of the yaw moment during the turning maneuvers are shown in Figure 12, for which the moment of the rudder angle deflecting to 35° is indicated.

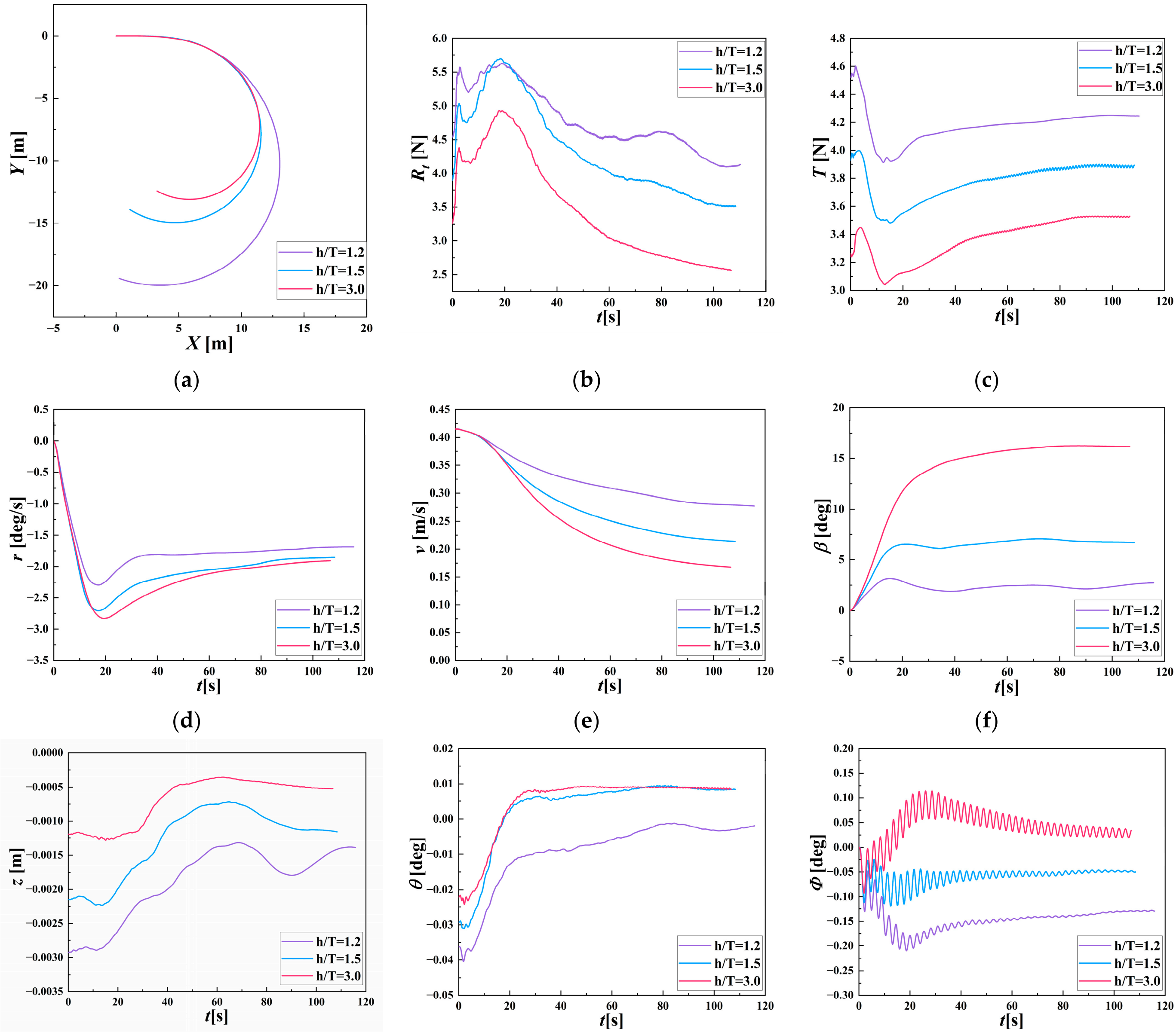

(a) (b) (c)

(d) (e) (f)

(g) (h) (i)

Figure 11. Turning trajectories and time series of motions for the turning maneuvers: (**a**) turning trajectories; (**b**) total resistance; (**c**) propulsion force; (**d**) yaw rate; (**e**) velocity; (**f**) drift angle; (**g**) heave motion; (**h**) pitch angle; (**i**) roll angle.

Table 13. Turning maneuver parameters for different water depths.

Parameter	Very Shallow Water	Shallow Water	Medium Deep Water
Tr [m]	9.854	7.012	5.577
Ad [m]	13.06	11.52	11.23
TD [m]	19.97	14.90	12.88
D [m]	18.88	13.50	10.53
φ_{steady} [deg]	−0.1290	−0.04865	0.02973
r_{steady} [deg/s]	−1.689	−1.866	1.923
β [deg]	2.731	6.758	16.19
V_{steady} [m/s]	0.2760	0.2172	0.1703
$\frac{u}{u_0}$ [-]	0.6650	0.5233	0.4102

D: the turning diameter in the steady turning state. φ_{steady}: the steady roll angle. r_{steady}: the steady yaw rate. V_{steady}: the steady velocity. $\frac{u}{u_0}$: the speed loss index.

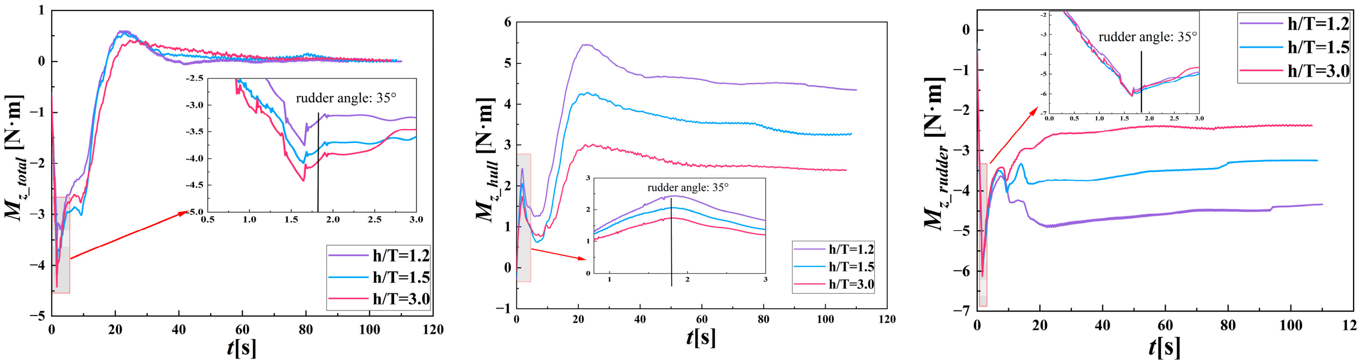

(**a**) (**b**) (**c**)

Figure 12. Time series of yaw moment during the turning maneuvers: (**a**) total yaw moment; (**b**) hull; (**c**) rudder.

The resistance of the ship increases greatly during steering and the transitional phase when the yaw rate and drift angle rise. The yaw rate decreases with a smaller depth–draft ratio, which leads to greater amplification of resistance, as shown in Table 13. Concretely, the resistance amplification in very shallow water when the rudder angle turns to 35° is 22%, while it grows to 34% in medium deep water. Meanwhile, the working state of the propeller changes due to the rudder deflection, and the thrust increases temporarily and then decreases rapidly. Hence, the ship speed is obviously reduced owing to the comprehensive effect of thrust and resistance. The speed loss index becomes smaller when the water is deeper, which is 67% in very shallow water and 40% in medium deep water. Correspondingly, the drift angle is smaller on account of the smaller speed loss index, while the drift angle in medium deep water is 6 times that in very shallow water.

Time series of the yaw moment during the turning maneuvers are shown in Figure 12, for which the moment of the rudder angle deflecting to 35° is indicated. The total yaw moment is divided into the yaw moment acting on the ship hull and the yaw moment acting on the rudder. During the steering phase, the total yaw moment decreases with shallower water, which is attributed to the lower yaw rate. Meanwhile, in the earlier stage of the transitional phase, the yaw moment in medium deep water is between that in shallow water and very shallow water. In the later stage of the transitional phase, the total yaw moment varies from a negative value to a positive value and changes monotonically with water depth. Meanwhile, the amplitude of angular velocity reaches its peak and starts to decrease. When the ship enters its steady turning stage, the total yaw moment at various water depths decreases to nearly zero, and the yaw rate tends to be stable. The turning yaw rates are close to each other in shallow water and medium deep water, with differences of no more than 3%. As seen in Figure 12b, the yaw moment acting on the hull shows a similar principle to the total yaw moment in the transitional phase, hence why the total yaw moment does not change monotonically with the water depth in the early stage of the transitional phase.

Figure 13 shows the flow field of the lateral velocity at X = 0.85L_{pp} while the rudder angle deflects to 35°. The lateral velocity represents an obvious asymmetry and increases for shallower water. Figure 14 shows the pressure field on the rudder when the rudder angle deflects to 35°. According to the results shown in Figure 12c, the rudder pressure field is barely affected by the water depth, and the pressure distribution at different water depths is the same, whether in shallow water or medium deep water. The yaw moment acting on the rudder varies little with water depth during the steering phase and the early stage of the transitional phase and is nearly the same for shallow water and medium deep water. However, during the later stage of the transitional phase and the steady turning phase, the yaw moment acting on the rudder declines with deeper water. In general, the yaw moment acting on the hull is the main reason for turning capability variations at different water depths during the steering and transitional phases.

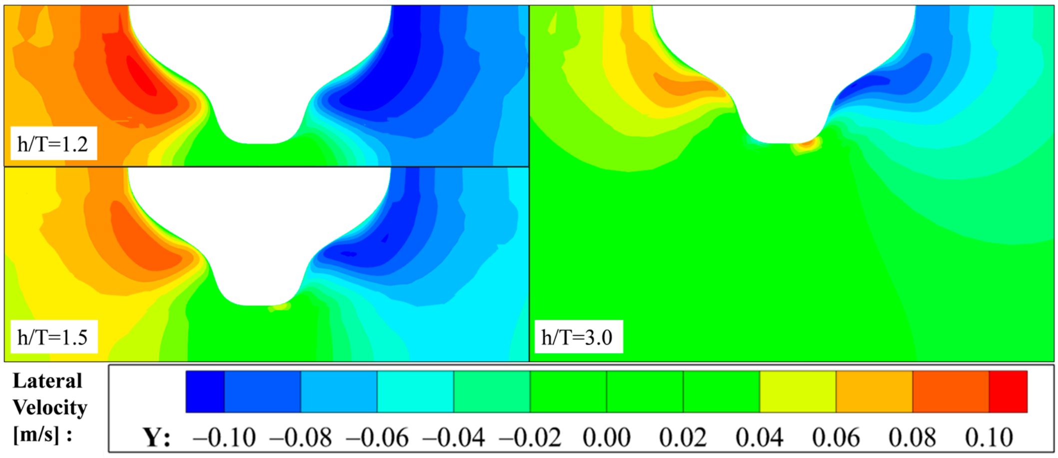

Figure 13. The lateral velocity field when rudder angle deflects to 35° (X = 0.85L_{pp}).

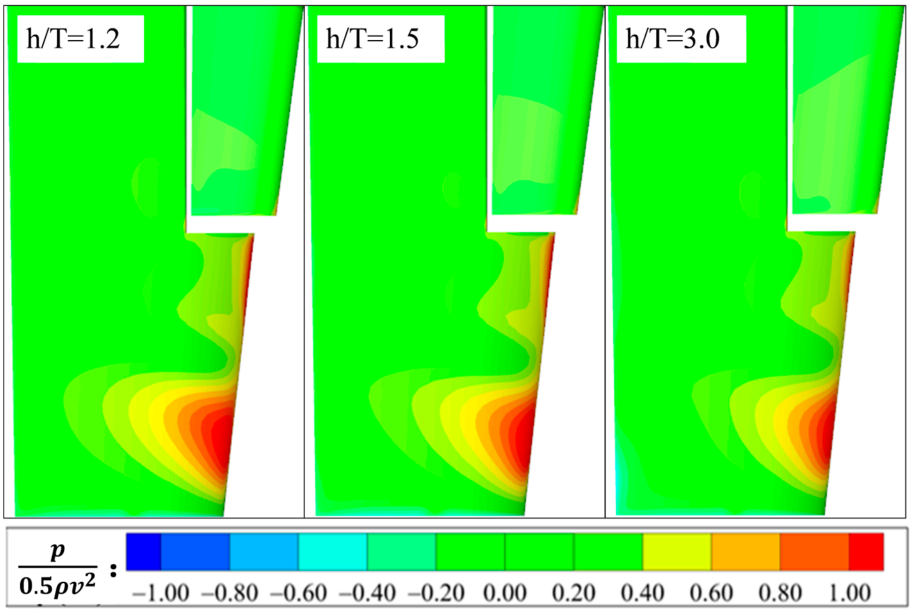

Figure 14. The pressure field on rudder when rudder angle deflects to 35°.

The free surface of the flow field when the ship turns to 180° is shown in Figure 15, which indicates greater wave-making in shallower water. From Figure 11, the amplitudes of heave and pitch motion decline obviously during the ship's turning phase. This may be caused by the pressure on the bottom of the ship rising due to the speed loss of the ship. Specifically, the amplitude of heave motion decreases by 50%, and the decreased amplitude of pitch motion is largely influenced by the water depth. The pitch amplitude decreases much more as the depth–draft ratio becomes smaller. Meanwhile, the pitch amplitudes in very shallow water and medium deep water are generally equal in the steady turning stage, and the trim on the bow during the self-propulsion phase changes to trim on the stern in this stage.

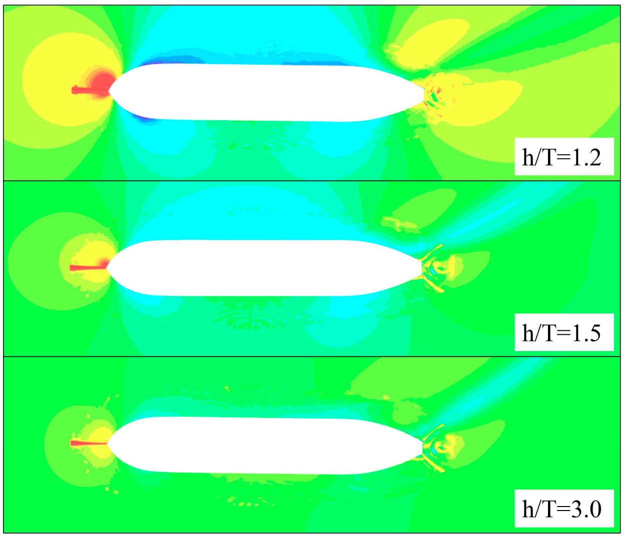

Figure 15. Free surface when ship turns to 180° at different water depths.

From the time series of roll motion exhibited in Figure 11, the ship heels inward obviously in very shallow water and shallow water, and the ship heels more acutely in the forward condition, while the ship heels inward and then it heels outward in medium deep water. This phenomenon is explained from the perspective of the rolling moment. The overall rolling moment acting on the ship is a combination of the ship rolling moment, the propeller rolling moment and the rudder rolling moment. The time series of the rolling moments are shown in Figure 16.

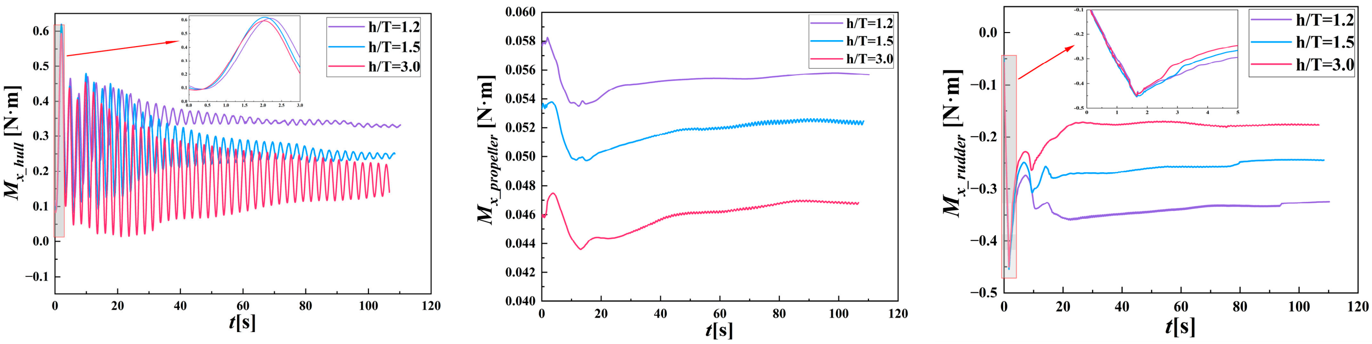

(**a**) (**b**) (**c**)

Figure 16. Time series of rolling moments during the turning maneuvers: (**a**) hull; (**b**) propeller; (**c**) rudder.

From Figure 16, it can be seen high-frequency fluctuations only appear in the time series of the hull rolling moment. And the amplitude of fluctuation increases as the depth–draft ratio increases, which is the main reason for roll angle fluctuations. The hull rolling moment increases as the depth–draft ratio increases. From the results shown in Figure 16b, it can be observed that the propeller rolling moment fluctuates consistently under different water conditions, and small variations occur during the steering stage. The rudder rolling moments are almost equal at different water depths during the steering stage, while they decrease as the water depth increases during the transitional phase and the steady turning stage. Generally, the ship's rolling moment is the maximum after steering, while the reverse rolling moment acting on the rudder is smaller; thus, the ship heels inward and then it heels outward in medium deep water.

5.2.2. Performance of the Propeller and Forces Acting on the Rudder during Turning Maneuvers

The propeller and rudder have an important impact on the turning performance of KVLCC2 in shallow water; therefore, the performance of the propeller and the forces acting on the rudder during turning maneuvers are studied in this section. Time series of the thrust coefficient K_T and torque coefficient K_Q are shown in Figure 17. The specific values of K_T, K_Q and the propeller efficiency η during self-propulsion and turning maneuvers at different water depths are shown in Table 14.

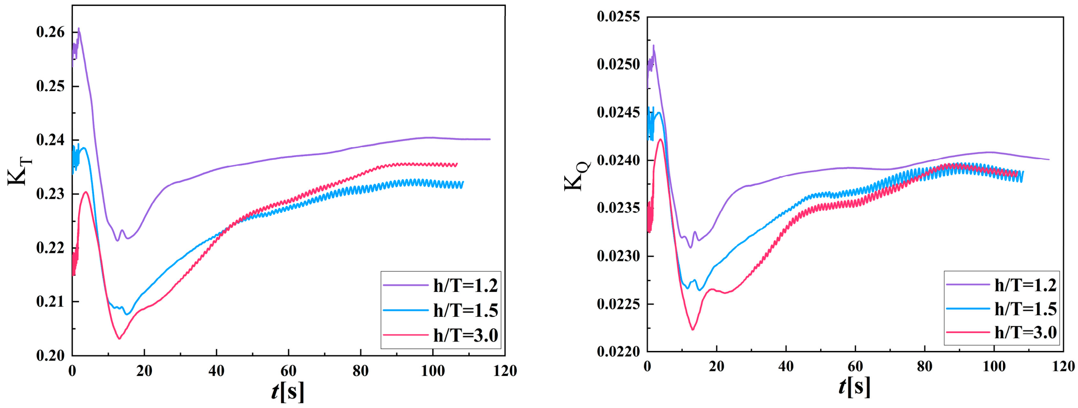

(**a**) (**b**)

Figure 17. Time series of K_T and K_Q at different water depths: (**a**) thrust efficient; (**b**) torque coefficient.

Table 14. Propeller performance of KVLCC2 in different depths of water in the steady turning stage.

Condition	h/T [-]	n [rps]	Self-Propulsion			Turning Maneuver		
			K_T [-]	K_Q [-]	η [-]	K_T [-]	K_Q [-]	η [-]
Very shallow water	1.2	7.756	0.2565	0.02499	0.4257	0.2401	0.02401	0.5000
Shallow water	1.5	7.551	0.2337	0.02423	0.5132	0.2317	0.02383	0.5270
Medium deep water	3.0	7.137	0.2182	0.02347	0.5647	0.2354	0.02386	0.5166

As seen in Table 14, the rudder deflections have an effect on K_T, K_Q and η of the propeller compared to turning maneuvers with self-propulsion. As seen in Figure 17, K_T and K_Q first increased and then decreased but finally stabilized within certain ranges. K_T and K_Q fluctuated violently and reached the minimum at about 15 s during the steering and transitional phases, while there was the maximum reduction in very shallow water. η increased in both very shallow water and shallow water during the steady turning stage compared with self-propulsion, while K_T and K_Q decreased by 6% and 4%, respectively, in very shallow water and decreased by 1% and 2%, respectively, in shallow water. Meanwhile, for medium deep water, η decreased by 9%, K_T increased by 8% and K_Q increased by 2%.

The velocities at KVLCC2's stern during self-propulsion and turning maneuvers when the ship turns 180° are shown in Figure 18. The velocity when the ship turns 180° was revised for clear comparisons. It can be observed that the speed flow field behind the propeller was influenced obviously by the deflection of the rudder, and notable differences can be seen for different water conditions. The deviation of the flow field reaches the maximum in medium deep water, which results from the largest drift angle under this condition. The resistance and lateral forces acting on the rudder during a turning maneuver are shown in Figure 19.

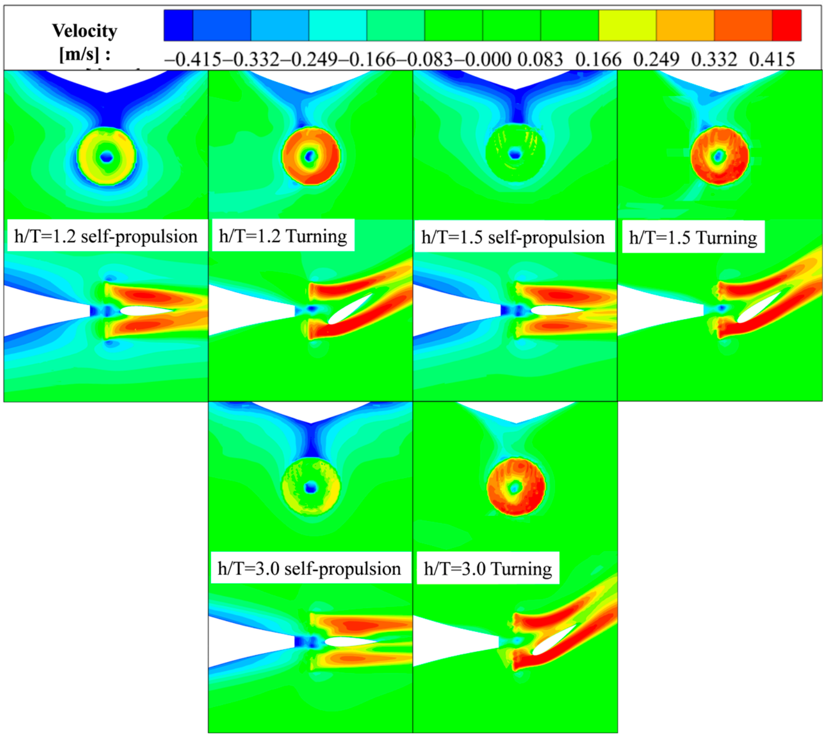

Figure 18. Velocity at the stern of KVLCC2 during self-propulsion and turning maneuvers (180°).

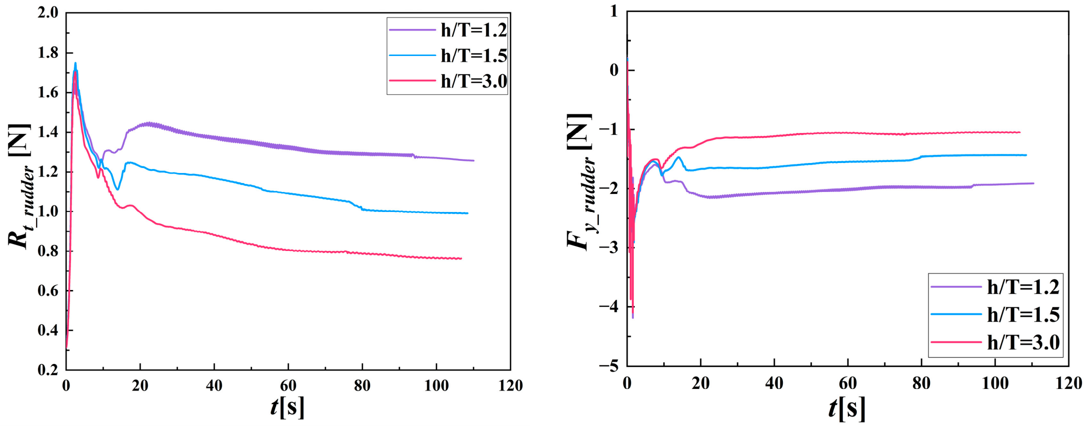

(**a**) (**b**)

Figure 19. Forces acting on rudder during turning maneuver: (**a**) resistance; (**b**) lateral force.

It can be observed that the resistance and lateral force surged during the steering stage, and both reached their peak value when finishing steering; there were also small differences for different water depths. Then, the forces acting on the rudder decreased during the transitional phase. During the steady turning stage, the forces acting on the rudder increased with a decrease in water depth, which resulted from the greater speed and drift angle when the depth of the water was shallower.

5.3. Results for the Zigzag Maneuver at Different Water Depths

5.3.1. Zigzag Indices of Zigzag Maneuvers at Different Water Depths

The indices for a zigzag maneuver under different water conditions are compared and assessed in this section. The ship was propelled to the self-propulsion point with a velocity of 0.415 m/s corresponding to Fn = 0.064 before steering. The maneuver consists of steering toward starboard and port at a given ship speed and rudder angle and then measuring the trajectory of the center of gravity of the ship. In this study, a 20/5 zigzag test with a rudder rate = 20.09°/s (corresponding to 2.32°/s at full scale) is performed. From the simulations, the first overshoot angle ψ_{ov1}, the second overshoot angle ψ_{ov2}, the first instance of the heading angle being equal to the rudder angle T_0, the first turn lag T_{L1}, the second turn lag T_{L2}, the maximum yaw rate r_{max} and the minimum yaw rate r_{min} could be obtained, as seen in Figure 20 and shown in Table 15.

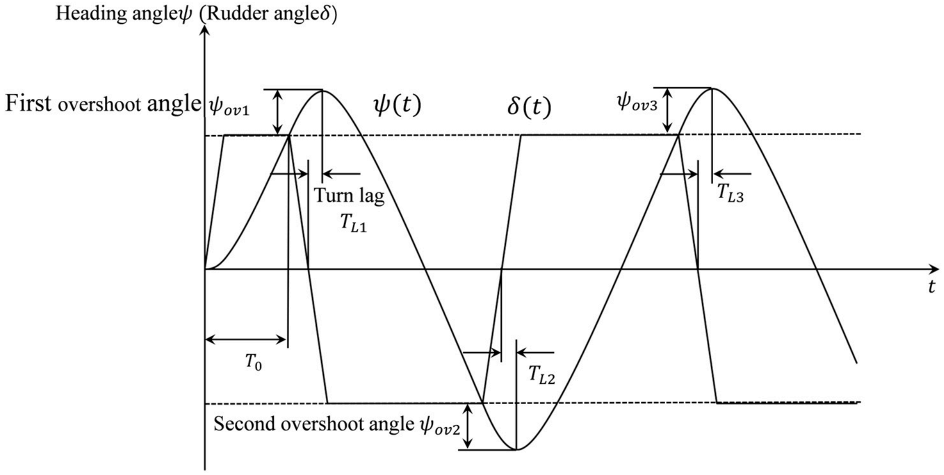

Figure 20. The characteristic definitions of the 20°/5° zigzag maneuver.

Table 15. Zigzag overshoot angle, turn lag and yaw rate at different water depths.

Parameter	Very Shallow Water	Shallow Water	Medium Deep Water
T_0	8.933	8.342	8.355
ψ_{ov1} [deg]	4.897	6.657	5.385
ψ_{ov2} [deg]	7.057	12.07	9.312
T_{L1} [s]	7.043	9.292	8.212
T_{L2} [s]	7.172	13.08	10.96
r_{max} [deg/s]	1.688	1.977	1.684
r_{min} [deg/s]	−1.730	−1.949	−1.798

From Figure 21 and Table 15, the ship's zigzag trajectories, heading angle, yaw rate, overshoot angle and turn lag do not vary monotonically with a change in water depth. The first and second overshoot angles increase from very shallow water to shallow water but decrease from shallow water to medium deep water. As a measurement of the ship's maneuver inertia, the change in the turn lag indicates that the maneuver inertia is smallest in very shallow water and medium in the medium deep water but largest in shallow water. The tendency for the overshoot angle and turn lag to vary during a zigzag maneuver is similar to the results found for the DTC (Duisburg Test Case) container ship studied using the MMG (Maneuvering Modeling Group) model (Liu et al. [13]).

As with the turning maneuver, the total yaw moment of the zigzag maneuver is divided into the yaw moment acting on the hull and that acting on the rudder, as shown in Figure 22. During the steering stage, the yaw moment acting on the hull varies monotonically with water depth, while the yaw moment acting on the rudder is influenced slightly by the water depth. Therefore, the total yaw moment in medium deep water grows larger, which is attributed to the appreciably increasing lateral velocity and drift angle. Meanwhile, during the transitional phase, the increasing lateral velocity and drift angle in medium deep water lead to a greater yaw moment acting on the hull than that in shallow water. Thus, the value of the total yaw moment in medium deep water is between that in shallow water and very shallow water, which represents a similar principle to the total yaw moment during the transitional phase of a turning maneuver. Differing from the turning maneuver, which will enter the steady turning phase, the rudder is steered reversely during the transitional phase of a zigzag maneuver. Therefore, the influence of the yaw moment not varying monotonically with water depth during the transitional phase gradually accumulates, which is the main reason for the non-monotonic variation in the overshoot angle and turn lag with water depth. The pressure field on the two sides of the rudder when the rudder angle turns to 20° for the first time is shown in Figure 23, which demonstrates that the water depth has a minor impact on the pressure field of the rudder, especially in shallow water and medium deep water.

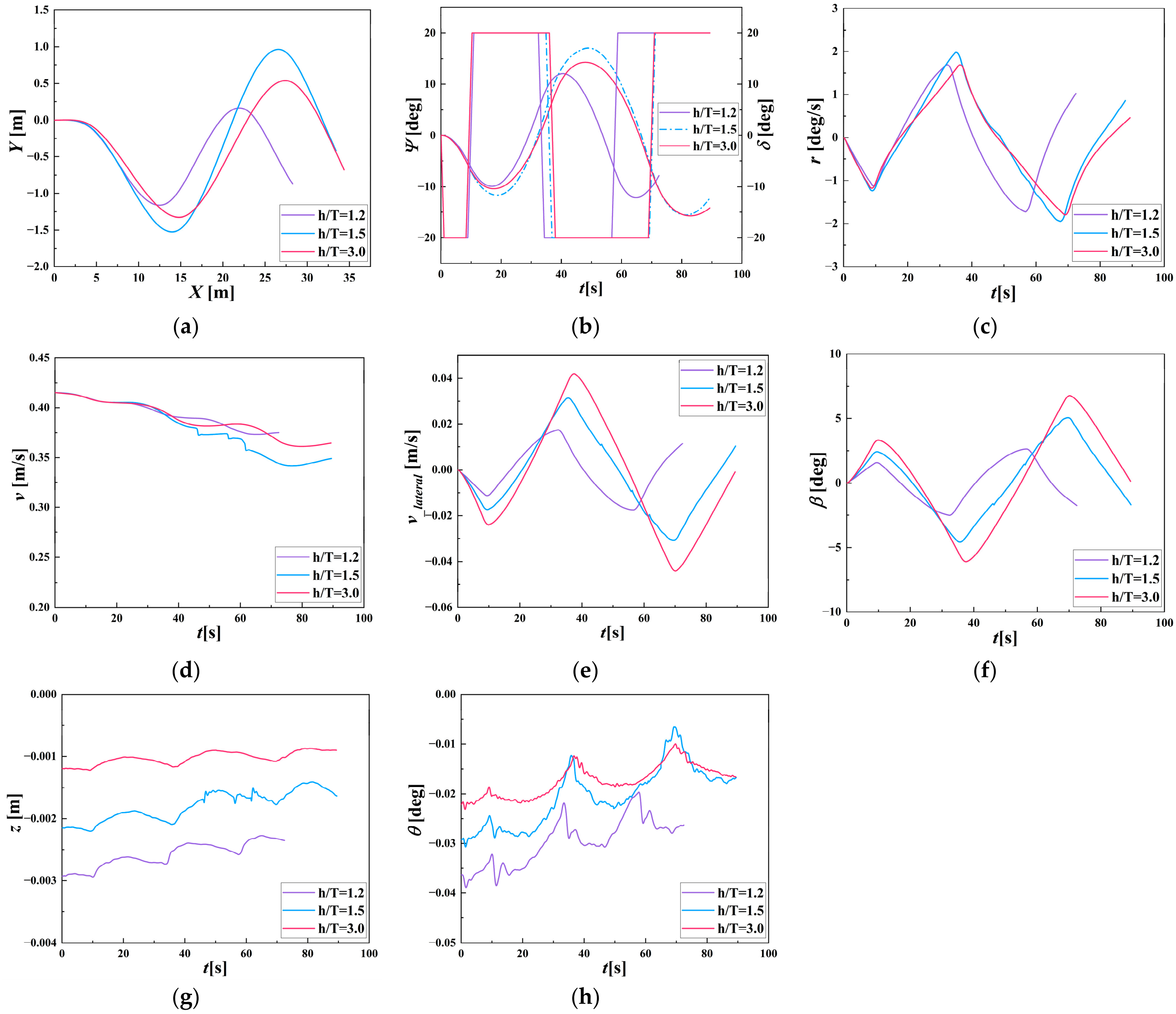

(**a**) (**b**) (**c**)

(**d**) (**e**) (**f**)

(**g**) (**h**)

Figure 21. Zigzag trajectories and time series of motions for the zigzag maneuvers: (**a**) zigzag trajectories; (**b**) heading angle and rudder angle; (**c**) yaw rate; (**d**) resultant velocity; (**e**) lateral velocity; (**f**) drift angle; (**g**) heave motion; (**h**) pitch angle.

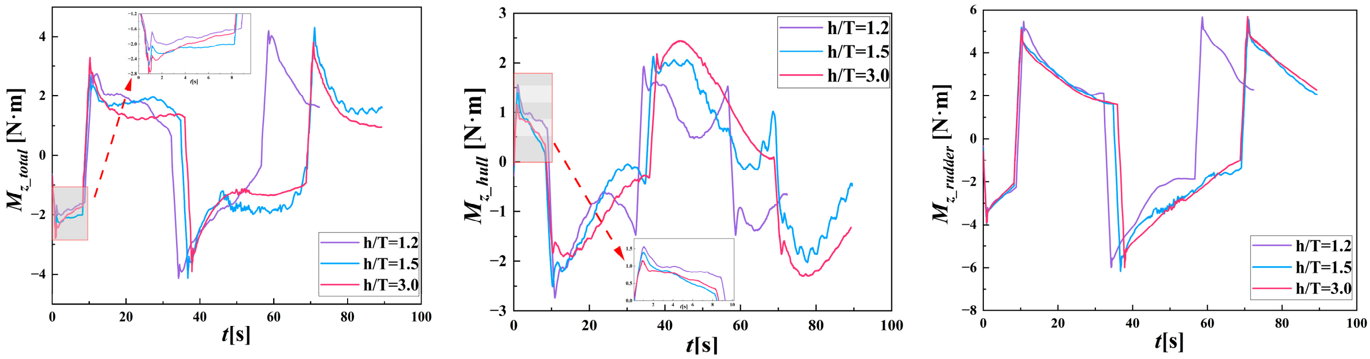

(**a**) (**b**) (**c**)

Figure 22. Time series of yaw moment during the zigzag maneuvers: (**a**) total; (**b**) hull; (**c**) rudder.

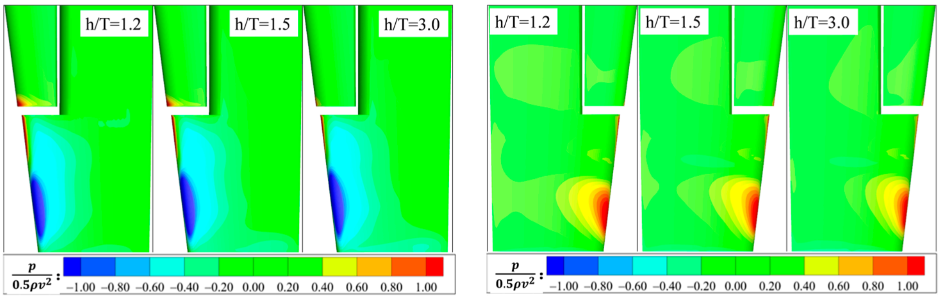

(**a**) (**b**)

Figure 23. Pressure field on two sides of the rudder corresponding to $\delta = 20^\circ$ at different water depths. (**a**) Port side; (**b**) starboard side.

5.3.2. Forces and Performance of the Propeller during Zigzag Maneuvers

As shown in Figure 21, the speed loss also does not vary monotonically with water depth, and it is largest in shallow water. Time series of the resistance and propulsion force are shown in Figure 24; the total resistance R_t is the resultant force of the hull resistance R_{hull} and the propulsion force T. The hull resistance fluctuates violently during the zigzag maneuver, in which the fluctuation of R_{hull} is the minimum in very shallow water, the maximum in shallow water and medium in medium deep water. Figure 24 indicates there are few differences in R_{hull} during the second steering. However, the propulsion force fluctuates more greatly when the water is shallower, and the fluctuation is much lower than the fluctuation in hull resistance. Thus, the difference in velocity under different water conditions is mainly affected by the hull resistance, and the speed loss is also the minimum in very shallow water, medium in medium deep water and the maximum in shallow water.

Figure 25 represents the time series of the lateral forces acting on the hull and rudder during the zigzag maneuver. It indicates that the lateral force varied with water depth monotonically, which caused the lateral velocity and drift angle to decline in shallower water, as seen in Figure 21. Furthermore, Figure 21 also shows that the heave amplitude increases with a decreasing water depth during the zigzag maneuver, but the value of pitch motion does not vary with water depth monotonically. The pitch amplitude reduced the most in shallow water, which results from the maximum speed loss under that condition. Figure 26 displays time series of the propeller thrust coefficient K_T and the torque coefficient K_Q during the zigzag maneuver. The amplitude of K_T gradually declines with an increasing water depth, and the difference between the maximum value and the minimum value of K_T is about 19% in very shallow water, 15% in shallow water and 11% in medium deep water. When compared with K_T, the fluctuation in K_Q is comparably small, and the variation between the lowest and greatest values of K_Q is 12% in very shallow water and 10% in shallow water and medium deep water.

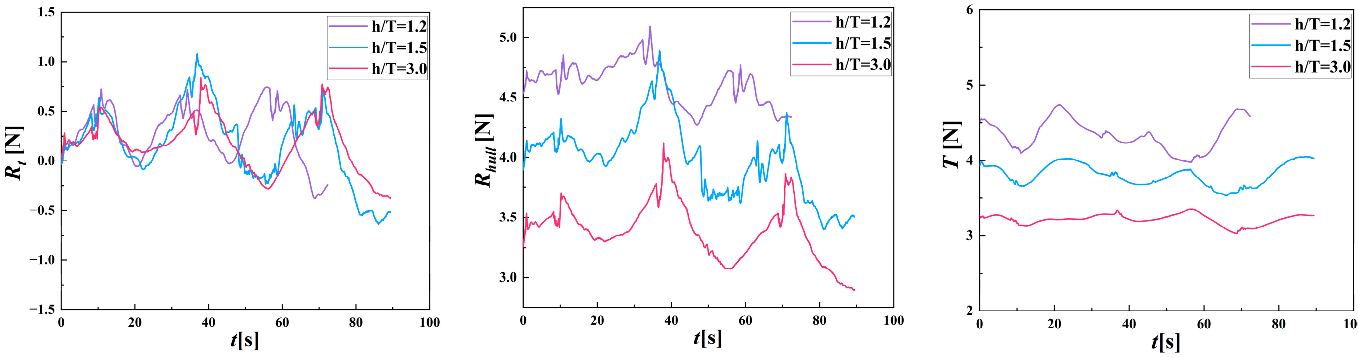

(**a**) (**b**) (**c**)

Figure 24. Time series of resistance and propulsion force during the zigzag maneuvers: (**a**) total resistance; (**b**) hull resistance; (**c**) propulsion force.

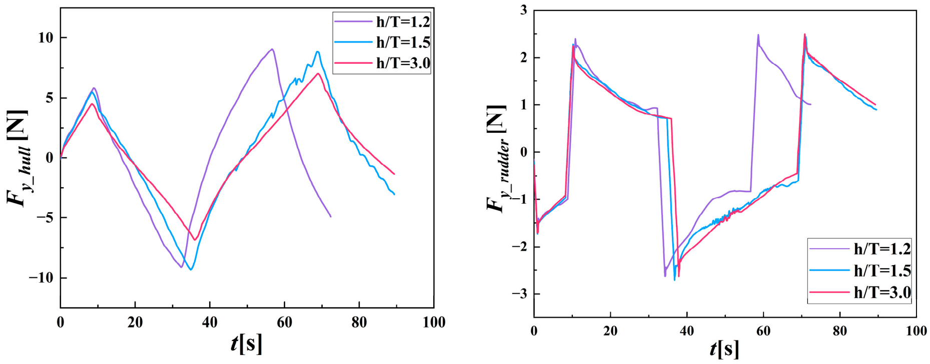

(**a**) (**b**)

Figure 25. Time series of lateral force during the zigzag maneuvers: (**a**) hull; (**b**) rudder.

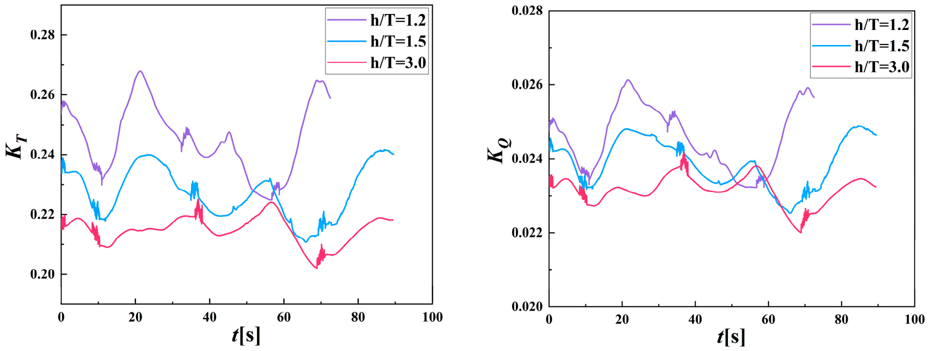

(**a**) (**b**)

Figure 26. Time series of propeller thrust coefficient (K_T) and propeller torque coefficient (K_Q) during the zigzag maneuvers: (**a**) K_T; (**b**) K_Q.

6. Conclusions

As shown from the literature in Section 1, the research on the maneuverability of ships in shallow waters currently uses model test methods, system-based empirical methods and viscous flow methods to obtain the hydrodynamic derivatives, as well as other indirect methods. In this paper, a viscous flow solver is used to directly predict the six-degrees-of-freedom maneuvering motions of a ship in different water depths, and comparison with the experimental data verifies the accuracy of the numerical method in predicting the maneuverability of a ship in shallow water. CFD computations at the model scale of KVLCC2 in very shallow water (h/T = 1.2), shallow water (h/T = 1.5) and medium deep water (h/T = 3.0) undergoing turning circle maneuvers with 35° rudder deflection and 20/5 zigzag maneuvers are presented. The parameters of the simulated turning circles are validated with the experimental results from the SIMMAN2020 website, and the accuracy of the numerical method can satisfy the requirements of ocean engineering.

For self-propulsion, a higher rotating speed is required compared to in shallower water in order to achieve the same velocity. Also, the amplitudes of heave and pitch motion also rise in shallower water, and the heave motion is affected more greatly by the shallow water effect than the pitch motion.

For turning maneuvers, the turning performance became poor in shallower water, as confirmed by the lower yaw rate and larger steady turning diameter. The steady turning diameter in very shallow water is 1.4 times that in shallow water and 1.8 times that in medium deep water, which results from the different forces acting on the hull and rudder during the steering phase. Meanwhile, the speed loss, drift angle and turning velocity decreased in the shallower water, and this speed loss is also attributed to obvious reductions in the heave and pitch amplitudes compared to with self-propulsion. The speed loss index is 67% in very shallow water and 40% in medium deep water, as well as the drift angle in medium deep water being 6 times of that in very shallow water. As for the performance of the propeller, η increased in both very shallow water and shallow water during the steady turning stage, compared with self-propulsion, while K_T and K_Q decreased by 6% and 4%, respectively, in very shallow water and decreased by 1% and 2%, respectively, in shallow water. Meanwhile, for medium deep water, η decreased by 9%, K_T increased by 8% and K_Q increased by 2%. Generally, the turning capability of KVLCC2 with 35° rudder deflection at low speed varied monotonically with water depth.

For zigzag maneuvers, the performance varied with water depth non-monotonically. The yaw rate, overshoot angle and turn lag increase from very shallow water to shallow water but decrease from shallow water to medium deep water, while the lateral velocity and drift angle increase with increasing water depth. As for the performance of the propeller, the amplitude of K_T gradually declines with an increasing water depth, and the difference between the maximum value and the minimum value of K_T is about 19% in very shallow water, 15% in shallow water and 11% in medium deep water. Meanwhile, compared with K_T, the fluctuation in K_Q is comparably small, and the variation between the lowest and greatest values of K_Q is 12% in very shallow water and 10% in shallow water and medium deep water.

Detailed analyses of the flow field, pressure field, hydrodynamic performance and ship motion reveal the influencing principles and mechanisms of water depth for ship maneuverability. In this paper, the flow field, pressure field, hydrodynamic performance and motion of the ship at different stages in different water depths are analyzed horizontally, and the interactions and influences between them are investigated to reveal the mechanisms of the influence of water depth on the parameters of a ship's maneuverability.

Author Contributions: Conceptualization, J.L.; Methodology, J.L.; Software, Q.W.; Formal analysis, J.L.; Investigation, J.L.; Resources, Q.W.; Writing—original draft, J.L.; Writing—review & editing, J.L., K.D. and X.W.; Supervision, X.W. All authors have read and agreed to the published version of the manuscript.

Funding: This research received no external funding.

Institutional Review Board Statement: Not applicable.

Informed Consent Statement: Not applicable.

Data Availability Statement: The data presented in this study are available on request from the corresponding author.

Conflicts of Interest: The authors declare no conflicts of interest.

References

1. Carrica, P.M.; Castro, A.M.; Stern, F. Self-propulsion computations using a speed controller and a discretized propeller with dynamic overset grids. *J. Mar. Sci. Technol.* **2010**, *15*, 316–330. [CrossRef]
2. EMSA. Annual Overview of Marine Casualties and Incidents. 2020. Available online: https://www.emsa.europa.eu/newsroom/latest-news/item/4266-annual-overview-of-marine-casualties-and-incidents-2020.html (accessed on 20 May 2024).
3. Sakamoto, N.; Carrica, P.M.; Stern, F. URANS simulations of static and dynamic maneuvering for surface combatant: Part 1. Verification and validation for forces, moment, and hydrodynamic derivatives. *J. Mar. Sci. Technol.* **2012**, *17*, 422–445. [CrossRef]
4. Carrica, P.M.; Ismail, F.; Hyman, M.; Bhushan, S.; Stern, F. Turn and zigzag maneuvers of a surface combatant using a URANS approach with dynamic overset grids. *J. Mar. Sci. Technol.* **2013**, *18*, 166–181. [CrossRef]
5. Woolliscroft, M.O.; Maki, K.J. A fast-running CFD formulation for unsteady ship maneuvering performance prediction. *Ocean Eng.* **2016**, *117*, 154–162. [CrossRef]
6. Wang, J.; Wan, D. CFD study of ship stopping maneuver by overset grid technique. *Ocean Eng.* **2020**, *197*, 106895. [CrossRef]
7. Shen, Z.; Wan, D.-C.; Carrica, P. RANS Simulations of Free Maneuvers with Moving Rudders and Propellers Using Overset Grids in OpenFOAM. In Proceedings of the SIMMAN Workshop on Verification and Validation of Ship Maneuvering Simulation Methods, Lyngby, Denmark, 8–10 December 2014; p. 77330.
8. Suzuki, R.; Ueno, M.; Tsukada, Y. Numerical simulation of 6-degrees-of-freedom motions for a manoeuvring ship in regular waves. *Appl. Ocean Res.* **2021**, *113*, 102732. [CrossRef]
9. Hamamoto, M.; Kim, Y.-S. A New Coordinate System and the Equations Describing Manoeuvring Motion of a Ship in Waves. *J. Soc. Nav. Archit. Jpn.* **1993**, *173*, 209–220. [CrossRef]
10. Kinaci, O.K.; Ozturk, D. Straight-ahead self-propulsion and turning maneuvers of DTC container ship with direct CFD simulations. *Ocean Eng.* **2022**, *244*, 110381. [CrossRef]
11. Cura-Hochbaum, A.; Uharek, S. Prediction of the manoeuvring behaviour of the KCS based on virtual captive tests. In Proceedings of the SIMMAN Workshop on Verification and Validation of Ship Maneuvering Simulation Methods, Lyngby, Denmark, 8–10 December 2014; p. 128.
12. Gadelho, J.F.M.; Rodrigues, J.M.; Lavrov, A.; Soares, C. Heave and sway hydrodynamic coefficients of ship hull sections in deep and shallow water using Navier-Stokes equations. *Ocean Eng.* **2018**, *154*, 262–276. [CrossRef]
13. Liu, Y.; Li, B.; Zou, L.; Zou, Z.J. Manoeuvrability Prediction for Container Ships in Deep and Shallow Waters. *J. Ship Mech.* **2019**, *23*, 280.
14. Tran Khanh, T.; Ouahsine, A.; Naceur, H.; El Wassifi, K. Assessment of ship maneuvrability by using a coupling between a nonlinear transient manoeuvring model and mathematical programming techniques. *J. Hydrodyn.* **2013**, *25*, 788–804. [CrossRef]
15. Du, P.; Ouahsine, A.; Toan, K.T.; Sergent, P. Simulation of ship maneuvering in a confined waterway using a nonlinear model based on optimization techniques. *Ocean Eng.* **2017**, *142*, 194–203. [CrossRef]
16. Tang, X.; Tong, S.; Huang, G.; Xu, G. Numerical investigation of the maneuverability of ships advancing in the non-uniform flow and shallow water areas. *Ocean Eng.* **2020**, *195*, 106679. [CrossRef]
17. Carrica, P.M.; Mofidi, A.; Eloot, K.; Delefortrie, G. Direct simulation and experimental study of zigzag maneuver of KCS in shallow water. *Ocean Eng.* **2016**, *112*, 117–133. [CrossRef]
18. Kim, D.Y.; Kim, S.-H.; Kim, S.-J.; Paik, K.-J. A study on the sensitivity analysis of the hydrodynamic derivatives on the maneuverability of KVLCC2 in shallow water. *Brodogradnja* **2017**, *68*, 1–22. [CrossRef]
19. Terziev, M.; Tezdogan, T.; Oguz, E.; Gourlay, T.; Demirel, Y.K.; Incecik, A. Numerical investigation of the behaviour and performance of ships advancing through restricted shallow waters. *J. Fluids Struct.* **2018**, *76*, 185–215. [CrossRef]
20. Lee, S.; Hong, C. Study on the course stability of very large vessels in shallow water using CFD. *Ocean Eng.* **2017**, *145*, 395–405. [CrossRef]
21. Simman. 2020. Available online: https://simman2020.kr/ (accessed on 20 May 2024).
22. PIANC. *Capability of Ship Manoeuvring Simulation Models for Approach Channels and Fairways in Harbours*; PIANC Report; PIANC: Brussels, Belgium, 1992; Volume 77.
23. Menter, F.R. Two-equation eddy-viscosity turbulence models for engineering applications. *AIAA J.* **1994**, *32*, 1598–1605. [CrossRef]
24. Carrica, P.M.; Wilson, R.V.; Stern, F. An unsteady single-phase level set method for viscous free surface flows. *Int. J. Numer. Methods Fluids* **2007**, *53*, 229–256. [CrossRef]
25. Tokgoz, E. A Cfd Study on the Propeller-Hull Interaction Flow in Waves Using Body-Force Distribution Model. Doctoral Dissertation, Osaka University, Osaka, Japan, 2015.
26. Feng, D.; Ye, B.; Zhang, Z.; Wang, X. Numerical Simulation of the Ship Resistance of KCS in Different Water Depths for Model-Scale and Full-Scale. *J. Mar. Sci. Eng.* **2020**, *8*, 745. [CrossRef]
27. Feng, D.; Yu, J.; He, R.; Zhang, Z.; Wang, X. Free running computations of KCS with different propulsion models. *Ocean Eng.* **2020**, *214*, 107563. [CrossRef]
28. Yu, J.; Yao, C.; Liu, L.; Zhang, Z.; Feng, D. Assessment of full-scale KCS free running simulation with body-force models. *Ocean Eng.* **2021**, *237*, 109570. [CrossRef]
29. Rogers, S.E.; Suhs, N.E.; Dietz, W.E. An Automated Preprocessor for Overset-Grid Computational Fluid Dynamics. *AIAA J.* **2003**, *41*, 1037–1045. [CrossRef]

30. Wilson, R.V.; Stern, F.; Coleman, H.W.; Paterson, E.G. Comprehensive Approach to Verification and Validation of CFD Simulations—Part 2: Application for Rans Simulation of a Cargo/Container Ship. *J. Fluids Eng.* **2001**, *123*, 803–810. [CrossRef]
31. Xing, T.; Stern, F. Factors of Safety for Richardson Extrapolation. *J. Fluids Eng.* **2010**, *132*, 061403. [CrossRef]
32. Naz, N. Numerical Simulation of Flow Around Ship Hull Considering Rudder-Propeller Interaction. Master's Thesis, Bangladesh University of Engineering and Technology, Dhaka, Bangladesh, 2017.
33. Deng, G.; Guilmineau, E.; Leroyer, A.; Queutey, P.; Visonneau, M.; Wackers, J. Simulation of Container Ship in Shallow Water at Model Scale and Full Scale. In Proceedings of the Third Chinese National CFD Symposium on Ship and Offshore Engineering, Dalian, China, 25–27 July 2014.
34. Kim, I.-T.; Kim, C.; Kim, S.-H.; Ko, D.; Moon, S.-H.; Park, H.; Kwon, J.; Jin, B. Estimation of the manoeuvrability of the KVLCC2 in calm water using free running simulation based on CFD. *Int. J. Nav. Archit. Ocean. Eng.* **2021**, *13*, 466–477. [CrossRef]